







# Ultrafast photo-induced carrier dynamics of perovskite quantum dots during structural degradation

CHEOL JO,<sup>1,†</sup>  DOKYUM KIM,<sup>2,†</sup>  CHANG-LYOUL LEE,<sup>2,3</sup>  AND DO-KYEONG KO<sup>1,4</sup> 

<sup>1</sup>Department of Physics and Photon Science, Gwangju Institute of Science and Technology, Gwangju 61005, Republic of Korea

<sup>2</sup>Advanced Photonics Research Institute, Gwangju Institute of Science and Technology, Gwangju 61005, Republic of Korea

<sup>3</sup>vsepr@gist.ac.kr

<sup>4</sup>dkko@gist.ac.kr

<sup>†</sup>These authors contributed equally to this work.

**Abstract:** In this study, the ultrafast photo-induced carrier dynamics of red-emitting PQDs during structural degradation was investigated using time-resolved transient absorption spectroscopy. The spectroscopic analysis revealed how the carrier dynamics varied when PQDs were exposed to a polar solvent. Three decay modes (carrier trapping, radiative carrier recombination and trap-assisted non-radiative recombination) were proposed to analyze the carrier dynamics of PQDs. The light-emitting property of PQDs is primarily influenced by radiative carrier recombination. This study demonstrates that structural degradation induced halide migration within PQDs and the formation of defects within the crystal lattice, leading to a proliferation of carrier trapping states. The increased trap states led to a reduction in carriers undergoing radiative carrier recombination. Additionally, PQDs degradation accelerated radiative carrier recombination, indicating a faster escape of carriers from excited states. Consequently, these factors hinder carriers remaining in excited states, leading to a decline in the light-emitting property of PQDs. Nevertheless, increasing an excitation fluence could reduce the carrier trapping mode and increase the radiative carrier recombination mode, suggesting a diminishment of the impact of carrier trapping. These findings offer a more comprehensive understanding of structural degradation of PQDs and can contribute to the development of PQDs with high structural stability.

© 2023 Optica Publishing Group under the terms of the [Optica Open Access Publishing Agreement](#)

## 1. Introduction

Quantum dots (QDs) have garnered considerable interest in the field of opto-electronics and wide range of applications [1,2]. Among the various types of QDs, halide perovskite quantum dots (PQDs) have emerged as promising materials in diverse fields, thanks to their exceptional optical characteristics, such as a high photoluminescence quantum yields (PLQYs), a narrow photoluminescence (PL) bandwidth, and easily tunable PL emission [3,4]. Due to these characteristics, PQDs exhibit impressive brightness and color purity, making them highly suitable for utilization in light-emitting diodes (LEDs) for next-generation display applications [5,6] and bio-imaging applications [7]. However, despite their excellent opto-electronic properties, PQDs face a significant challenge in terms of their poor structural stabilities because they are readily degraded and decomposed by the effect of environmental factors, such as moisture and oxygen [8–10].

In the case of red-emitting PQDs, a mixed halide composition of bromine (Br) and iodine (I) is required, as illustrated in Fig. S1a. Numerous studies have reported on the degradation arising

from the instability of I<sup>-</sup> ions in mixed halide perovskites designed for red-emitting materials [11–13]. Particularly, due to easy migration of I<sup>-</sup> ions within the perovskite crystal lattice (Fig. S1b), the defect formation occurs easily, leading to poor structural stabilities [14,15]. The presence of defects within the perovskite crystal lattice leads to the proliferation of trap states that capture the photo-induced charge carriers, consequently degrading the optical properties of PQDs [16]. For this reason, numerous researchers have investigated the structural degradation in red-emitting CsPb(Br<sub>1-x</sub>I<sub>x</sub>)<sub>3</sub> QDs [17–19]. However, the underlying structural degradation mechanism has remained poorly understood, because previous studies about structural degradation of PQDs have mainly relied on macroscopic and steady-state analyses. Conversely, there have been extensive researches on ultrafast and time-resolved analyses of photo-induced carrier dynamics in perovskite materials using transient absorption (TA) spectroscopy [20–25]. Nevertheless, these TA spectroscopy studies did not show clear relationship between the structural stability and the carrier dynamics during degradation of PQDs.

Motivated by these considerations, this study deeply investigated the photo-induced charge carrier dynamics of red-emitting core-shell CsPb(Br<sub>0.25</sub>I<sub>0.75</sub>)<sub>3</sub>@SiO<sub>2</sub> QDs during structural degradation, to reveal the effect of defects within perovskite lattice and to gain insights into the structural degradation process of PQDs at the ultrafast timescale and carrier-level. To maintain a controlled environment for structural degradation, the PQDs solution was mixed with a moderately polar solvent, butanol (BuOH). BuOH is not the common choice, because most of studies have predominantly used H<sub>2</sub>O as polar solvent for inducing structural degradation of PQD. However, we intended to utilize various experimental methods including photoluminescence (PL), transmission electron microscopy (TEM), X-ray diffraction (XRD), and TA spectroscopy to analyze the structural degradation of PQDs. Therefore, it was necessary to maintain a condition that would have a minimal impact during a series of measurements to ensure reproducibility. The use of H<sub>2</sub>O as the polar solvent for structural degradation of PQDs would have led to significant variation in the results of measurements due to the time required for each measurement or time intervals between measurements. For this reason, BuOH, with lower polarity compared to H<sub>2</sub>O, was chosen to slow down the structural degradation of PQDs. Furthermore, an additional advantage of BuOH is its miscibility with toluene, the dispersion solvent for PQDs used in this study, while H<sub>2</sub>O does not mix well with toluene. This ensures the homogeneous degradation of PQDs even in solution, which was essential for maintaining consistent observations regardless of measurement positions. Subsequently, TA measurements were conducted on the PQDs solution with gradually increasing the exposure time to BuOH in order to progressively increase the effect of structural degradation. Consequently, the optical characteristics of the red-emitting PQDs were elucidated based on the ultrafast spectroscopic analysis about the photo-induced charge carrier dynamics varying with increasing BuOH exposure time.

## 2. Experimental methods

### 2.1. Preparation of core-shell CsPb(Br<sub>0.25</sub>I<sub>0.75</sub>)<sub>3</sub>@SiO<sub>2</sub> QDs

PQDs were synthesized using a modified hot-injection method [19]. The schematic diagram of the modified hot-injection process is illustrated in Fig. S2. Cs-Oleate was prepared by adding 0.6 mmol of Cs<sub>2</sub>CO<sub>3</sub> (99%, Sigma-Aldrich), 0.7 mL of oleic acid (OA, 90%, Sigma-Aldrich), and 8 mL of 1-octadecene (ODE, 90%, Sigma-Aldrich) into a 25 mL two-neck flask. The Pb-pot was prepared by adding 0.08 mmol of PbBr<sub>2</sub> (98%, Sigma-Aldrich) and 0.24 mmol of PbI<sub>2</sub> (99.999%, Sigma-Aldrich) into another 100 mL two-neck flask containing 15 mL of ODE. The flasks were then degassed under vacuum at 100 °C for 30 minutes. After degassing, the gas lines were connected to N<sub>2</sub>. Next, 1.5 mL of OA, 0.4 mL of oleylamine (OAm, 70%, Sigma-Aldrich), and 1.2 mL of 3-aminopropyltriethoxysilane (APTES, 98%, Sigma-Aldrich) were added to the Pb-pot to dissolve the Pb precursor. The temperature of the Pb-pot was then raised to 165 °C, and the prepared Cs-Oleate (preheated at 150 °C) was quickly injected. The crude solution

was quenched in an ice bath after  $\sim 20$  seconds of reaction. To collect the purified core-shell  $\text{CsPb}(\text{Br}_{0.25}\text{I}_{0.75})_3 @ \text{SiO}_2$  QDs, the supernatant solution was first centrifuged with acetone at 8000 rpm for 3 minutes. Then, the precipitates were centrifuged with methyl acetate at 15000 rpm for 5 minutes. Finally, the precipitates were dispersed in toluene. The concentration of PQDs in the solution was measured to be  $\sim 8.75$  mg/ml.

## 2.2. Transient absorption spectroscopy (TAS)

Ultrafast photo-induced charge carrier dynamics of  $\text{CsPb}(\text{Br}_{0.25}\text{I}_{0.75})_3 @ \text{SiO}_2$  QDs was investigated using time-resolved TA spectroscopy with a pump-probe setup based on a femtosecond laser system. Schematic diagram of the ultrafast TA spectroscopy system is presented in Fig. S3. The TA spectroscopy system was based on seed pulses from a Ti:Sapphire laser (MaiTai, Spectra-Physics) and a femtosecond Ti:Sapphire laser amplifier system (Spitfire Ace PA, Spectra-Physics). Two Q-switched lasers (Empower, Spectra-Physics) were employed for pumping the output pulses. The generated fundamental pulse exhibited a full width at half maximum of  $\sim 36$  fs in temporal profile and  $\sim 26$  nm in spectral profile centered at 805 nm with a repetition rate of 1 kHz. The fundamental beam was divided into two paths: a pump beam and a probe beam. The pump beam underwent frequency doubling through second harmonic generation. The probe beam was used for supercontinuum generation to obtain a broadband wavelength range from visible to near-infrared (450  $\sim$  1000 nm). The polarization angle between the pump and probe beams was adjusted to the magic-angle ( $54.7^\circ$ ). The PQDs solution was filled in a quartz cuvette with 1 mm optical pathlength, and the cuvette was placed in a cuvette holder where the focused pump and probe beams overlapped at room temperature (293 K).

## 2.3. Photoluminescence (PL)

Photoluminescence (PL) spectra of the PQDs solution were measured using two monochromator systems (SP-2150i and SP-2300i, Acton) equipped with a photomultiplier tube (PMT, Acton PD471) and a Xenon lamp as an excitation light source. The photoluminescence quantum yields (PLQYs) of PQDs were calculated relative to Rhodamine 101 with a PLQY of  $\sim 97\%$  in ethanol.

## 2.4. Transmission electron microscopy (TEM) and energy dispersive X-ray spectroscopy (EDS)

Average particle sizes and selected area diffractions of PQDs were observed using transmission electron microscopy (Tecnai G2 F30 S-Twin 300 kV). Compositional analysis was performed using the Octane in Elite EDS system.

## 2.5. X-ray diffraction (XRD)

The phase, crystal structure indexing, and d-spacing of PQDs were determined from X-ray diffraction patterns obtained using a Rigaku D/max-2500 diffractometer with  $\text{Cu K}\alpha$  radiation ( $\lambda = 1.5418 \text{ \AA}$ ) operating at 40 kV and 100 mA.

# 3. Results and discussion

## 3.1. Steady-state spectroscopy of $\text{CsPb}(\text{Br}_{0.25}\text{I}_{0.75})_3 @ \text{SiO}_2$ QDs degraded by BuOH exposure

10 vol% of BuOH was added to  $\text{CsPb}(\text{Br}_{0.25}\text{I}_{0.75})_3 @ \text{SiO}_2$  QDs solution for structural degradation. Photoluminescence (PL) spectra of the red-emitting PQDs with increasing BuOH exposure time are presented in Fig. 1(a). The photoluminescence quantum yields (PLQYs) and the maximum PL emission peaks as a function of BuOH exposure time are displayed in Fig. 1(b). In addition to the PL spectra, UV-vis absorption spectra are also presented in Fig. S4. As the BuOH exposure time increased, the PLQYs decreased from  $\sim 60\%$  to  $\sim 23\%$ . The decrease in PLQYs indicates

that the addition of BuOH induced structural degradation in the  $\text{CsPb}(\text{Br}_{0.25}\text{I}_{0.75})_3 @ \text{SiO}_2$  QDs. In addition to the decrease in PLQYs, blue-shifts in the PL spectra and the UV-vis absorption spectra indicate an increase in the bandgap, which results from a band-edge transition induced by the structural degradation of PQDs. The change in the bandgap can be explained by the quantum confinement effect [26]. The quantum confinement effect suggests that the bandgap is influenced by a particle size. Therefore, the blue-shifted UV absorption and PL emission of PQDs can be attributed to a reduction in particle size during the process of structural degradation.

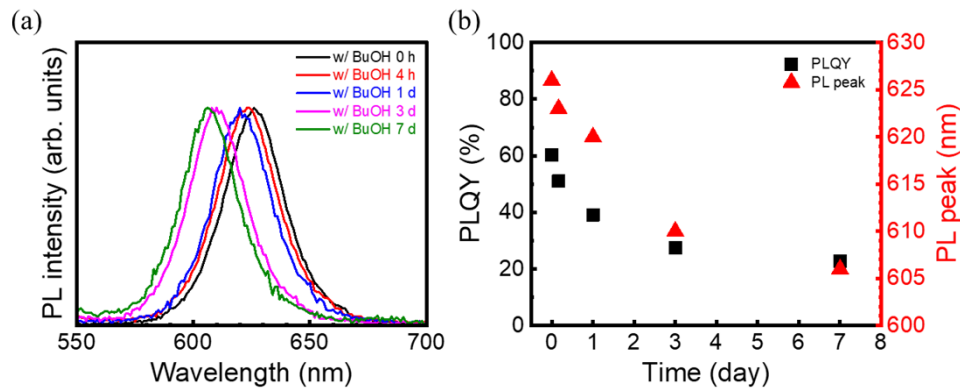


**Fig. 1.** (a) Photoluminescence (PL) spectra, and (b) photoluminescence quantum yields (PLQYs) and maximum PL emission peaks of  $\text{CsPb}(\text{Br}_{0.25}\text{I}_{0.75})_3 @ \text{SiO}_2$  QDs as a function of BuOH exposure time.

In order to investigate the change in particle size of  $\text{CsPb}(\text{Br}_{0.25}\text{I}_{0.75})_3 @ \text{SiO}_2$  QDs, the transmission electron microscopy (TEM) experiments were conducted and the TEM images with different BuOH exposure times are displayed in Fig. 2(a) ~ e. The average particle sizes of PQDs corresponding to different BuOH exposures are presented in the insets. The average particle size of  $\text{CsPb}(\text{Br}_{0.25}\text{I}_{0.75})_3 @ \text{SiO}_2$  QDs was observed to decrease as BuOH exposure time increased. In the absence of BuOH exposure (designated as 0 h), the average particle size of PQDs was measured to be ~ 20.89 nm. After 7 days (7 d) of BuOH exposure, the average particle size was reduced to ~ 14.99 nm. This observation indicates a gradual decrease in particle size (depicted in Fig. 2(f)). Additionally, the fast Fourier transform (FFT) patterns obtained from high-resolution TEM images, as presented in Fig. 3, suggest a reduction in lattice *d*-spacing without any change in the crystal structure (all remained orthorhombic).

The X-ray diffraction (XRD) patterns for analyzing the crystal structure of PQDs are presented in Fig. 4(a). When compared to the orthorhombic  $\text{CsPbBr}_3$  (reference number 98-009-7851 in ICSD; Inorganic Crystal Structure Database), the XRD patterns exhibited peak shifts, indicating a change in lattice parameters. Nevertheless, the overall shape of the patterns remained similar to that of the orthorhombic  $\text{CsPbBr}_3$  reference, suggesting that PQDs maintains an orthorhombic crystal structure throughout all exposure times. Additionally, it was observed that the XRD peaks around 30 degrees (depicted in Fig. 4(b)) exhibited a gradual high-angle shift with increasing BuOH exposure time. The peaks correspond to the (004) and (220) planes of PQDs. By applying Bragg's law, a decrease in *d*-spacing was found, as shown in Fig. 4(c). The results from the XRD patterns align with the TEM results shown in Figs. 2 and 3. Therefore, these findings demonstrate that the structural degradation process is associated with the decrease in both *d*-spacing and particle size of PQDs.

Energy Dispersive X-ray Spectroscopy (TEM-EDS) analysis was conducted to quantify the halide composition of PQDs with different BuOH exposure times. The atomic fractions of bromine (Br) and iodine (I) as a function of BuOH exposure time are presented in Fig. 5. In



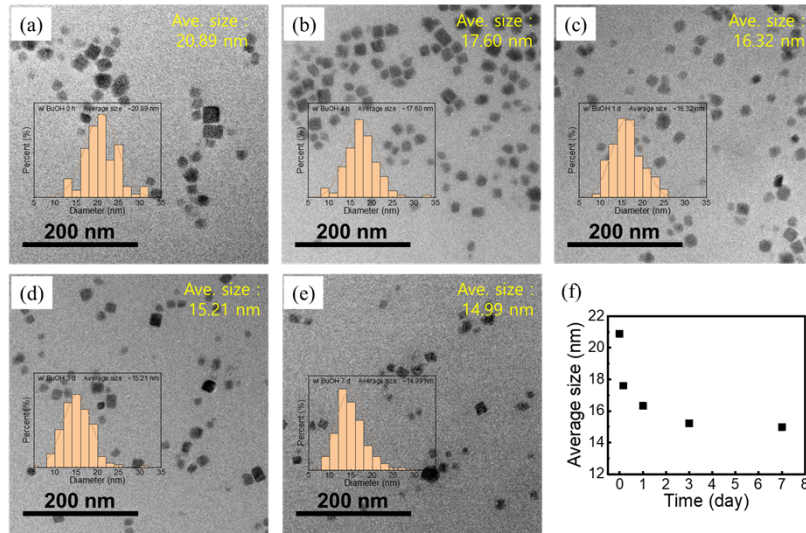


**Fig. 2.** Transmission electron microscopy (TEM) images of CsPb(Br<sub>0.25</sub>I<sub>0.75</sub>)<sub>3</sub>@SiO<sub>2</sub> QDs with different BuOH exposure times: (a) 0 h, (b) 4 h, (c) 1 d, (d) 3 d, and (e) 7 d. The particle size distributions are shown in insets. (f) The change in particle size of the CsPb(Br<sub>0.25</sub>I<sub>0.75</sub>)<sub>3</sub>@SiO<sub>2</sub> QDs as a function of BuOH exposure time.

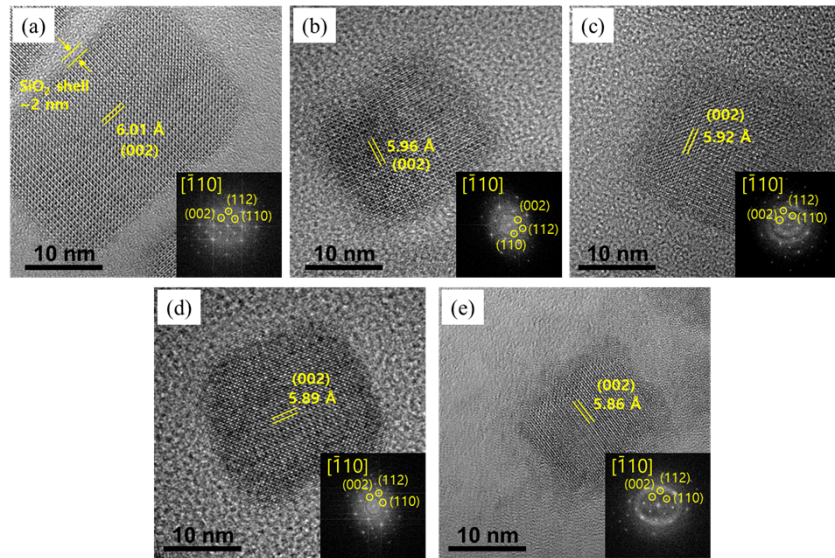


**Fig. 3.** High magnification TEM images of CsPb(Br<sub>0.25</sub>I<sub>0.75</sub>)<sub>3</sub>@SiO<sub>2</sub> QDs with different BuOH exposure times: (a) 0 h, (b) 4 h, (c) 1 d, (d) 3 d, and (e) 7 d. The insets show the fast Fourier transform (FFT) patterns obtained from the respective images.

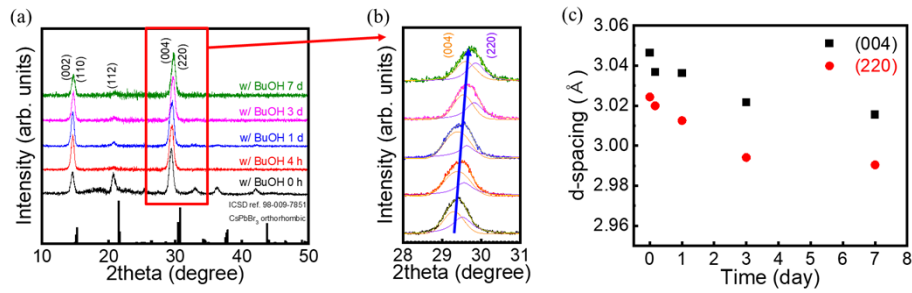


**Fig. 4.** (a) X-ray diffraction (XRD) patterns of  $\text{CsPb}(\text{Br}_{0.25}\text{I}_{0.75})_3@ \text{SiO}_2$  QDs with different BuOH exposure times. (b) Magnified view focused on the (004) and (220) peak region. (c) The  $d$ -spacing calculated from the  $2\theta$  values of the (004) and (220) peaks.

PQDs without BuOH exposure (0 h), the atomic fraction of Br was  $\sim 45\%$ , while the atomic fraction of I was  $\sim 55\%$ . However, with an increase of BuOH exposure time, the atomic fraction of I gradually decreased, and the atomic fraction of Br showed a continuous increase. After 7 days, the atomic fraction of Br reached  $\sim 72\%$ , while the atomic fraction of I decreased to  $\sim 28\%$ . Considering no additional halide supplement from an external source, this phenomenon is expected to arise due to the relatively rapid decrease in the concentration of I compared to Br. It indicates  $\text{I}^-$  migration within the crystal lattice [19]. The decrease in both particle size (Fig. 2) and  $d$ -spacing (Figs. 3 and 4) can be attributed to the  $\text{I}^-$  migration induced by BuOH exposure. Since iodine has a larger ionic radius (220 pm) compared to Br (196 pm), the decrease in both particle size and  $d$ -spacing occurs with increasing BuOH exposure time. Previous studies have explored bandgap engineering through the adjustment of PQDs' halide composition [27,28]. Therefore, the change in PQDs' bandgap could be induced by the  $\text{I}^-$  migration, leading to the blue-shift in the absorption edge and the PL peak (Figs. S4 and 1). Moreover, the  $\text{I}^-$  migration within PQDs forms vacancies within the perovskite crystal lattice, leading to the proliferation of defects and an accompanying increase in trap state densities [14–16]. This phenomenon ultimately results in the decrease in PLQYs of PQDs (Fig. 1).

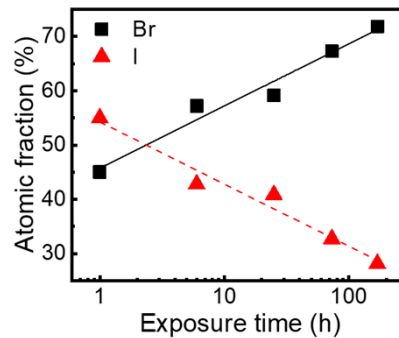


**Fig. 5.** Atomic fractions between bromine (Br) and iodine (I) of  $\text{CsPb}(\text{Br}_{0.25}\text{I}_{0.75})_3@ \text{SiO}_2$  QDs as a function of BuOH exposure time, determined from TEM-EDS analysis.

### 3.2. Time-resolved spectroscopy of $\text{CsPb}(\text{Br}_{0.25}\text{I}_{0.75})_3@ \text{SiO}_2$ QDs degraded by BuOH exposure

After discovering that the proliferation of trap states by  $\text{I}^-$  migrations is the primary cause of structural degradation of PQDs, the ultrafast photo-induced charge carrier dynamics of core-shell

CsPb(Br<sub>0.25</sub>I<sub>0.75</sub>)<sub>3</sub>@SiO<sub>2</sub> QDs was investigated by using a TA spectroscopy system, because the formation of trap states would be expected to influence charge carrier behaviors. The differential absorption ( $\Delta A$ ) spectra of PQDs with different BuOH exposure times were obtained by exciting the CsPb(Br<sub>0.25</sub>I<sub>0.75</sub>)<sub>3</sub>@SiO<sub>2</sub> QDs solution with a 400 nm excitation pump. The differential absorption ( $\Delta A$ ) measurements were performed with applying a delay time between the pump and probe, because the pump-probe delay at which the TA signals reach their maximum amplitude can vary with factors such as TA rising time [25,29] and hot-carrier relaxation [30,31]. In the differential absorption spectra shown in Fig. 6(a), the red-emitting PQDs exhibit two distinct curves at all BuOH exposure times. The negatively-signed curve is observed below 700 nm, while the positive curve is observed above 700 nm. The negative curve corresponds to photo-induced transient ground-state bleaching (GSB) of the band-edge. The positive absorption region indicates the additional excitation of carriers in excited states to higher unoccupied states, known as excited-state absorption (ESA). Similar to the PL spectra (Fig. 1), it was observed that the area of the GSB region undergoes a reduction, and the peak shifted towards shorter wavelengths (blue-shifted) as BuOH exposure time increased. The reduction of the GSB area corresponds to the drop in PLQYs caused by structural degradation of PQDs, and the blue-shift in the wavelength spectrum is attributed to the change in the bandgap (Fig. 1 and Fig. S4). To enhance the clarity of the blue-shift in the GSB peaks with increasing BuOH exposure time, normalized TA ( $\Delta A/A$ ) spectra of PQDs are presented in Fig. 6(b). However, conducting a comparative analysis solely based on differential absorption spectra and TA spectra is not sufficient for the characterization of PQDs with different BuOH exposure times. Therefore, it is necessary to investigate the kinetic traces at each GSB peak of TA spectra in order to gain a deeper understanding of the carrier dynamics of PQDs during structural degradation.

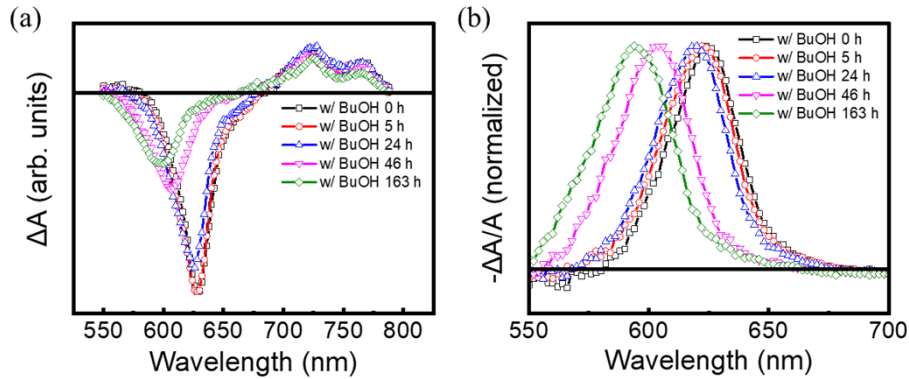


**Fig. 6.** (a) Differential absorption ( $\Delta A$ ) and (b) transient absorption ( $\Delta A/A$ ) spectra of CsPb(Br<sub>0.25</sub>I<sub>0.75</sub>)<sub>3</sub>@SiO<sub>2</sub> QDs at pump-probe delay time of 21.6 ps using a 400 nm excitation pump with a fluence of 25  $\mu\text{J}/\text{cm}^2$ .

TA kinetic traces were obtained by measuring TA signals at the wavelengths corresponding to their GSB peaks in the TA spectra and with a series of pump-probe time delays. Each TA kinetic trace represents the average of at least 3 up to 8 measurements, and these traces are presented in Fig. S5. For a spectroscopic analysis, the TA kinetic traces were normalized and bi-exponential decay fits were applied using Eq. (1),

$$y(t) = A_1 e^{-\frac{t-\tau_0}{\tau_1}} + A_2 e^{-\frac{t-\tau_0}{\tau_2}} + y_0, \quad (\tau_1 < \tau_2). \quad (1)$$

where  $y$  represents the TA kinetic signal at a pump-probe delay of  $t$ . The normalized TA decay kinetic traces of PQDs excited with pump fluences of 10 and 20  $\mu\text{J}/\text{cm}^2$  are presented in Fig. 7(a) and (b), respectively. The fitting parameters of the TA kinetic traces with excitation fluences of

10 and 20  $\mu\text{J}/\text{cm}^2$  are summarized in Table 1 and Table 2, respectively. The arrows in Fig. 7(a) and (b) indicate the direction of increasing BuOH exposure time, and the solid lines represent the bi-exponential decay fit lines for the TA kinetic traces (the plots featuring only the fit lines are depicted in Fig. S6). At first glance, the decay of the TA signal appears to be simply accelerated with increasing BuOH exposure time, meaning that the TA kinetic traces follow a mono-exponential decay. However, the actual trend of the change in TA kinetic traces is more complex, because the kinetic traces consist of two decay terms and a constant term. Therefore, it is necessary to consider not only the decay lifetimes ( $\tau_1$  and  $\tau_2$ ), but also the coefficients ( $A_1$ ,  $A_2$ , and  $y_0$ ). To separately analyse the two decay terms, the TA kinetic traces are divided into two parts: the early-time regime (0 ~ 50 ps) for distinguishing the fast decay mode ( $A_1$ ,  $\tau_1$ ), and the late-time regime (50 ~ 1100 ps) for the slow decay mode ( $A_2$ ,  $\tau_2$ ). The early-time regime in the TA kinetic traces is particularly illustrated in the inset of Fig. 7(a) and (b). Based on the fitting parameters presented in Table 1 and Table 2, it was confirmed that the exposure to BuOH leads to an increase in the fraction of the fast decay mode ( $A_1$  increases) and a decrease in the lifetime of the fast decay mode ( $\tau_1$  decreases) in the early-time regime. In the late-time regime, the fraction of the slow decay mode decreases ( $A_2$  decreases) while the decay lifetime decreases ( $\tau_2$  decreases) with increasing BuOH exposure time.

**Table 1. Fitting parameters of bi-exponential decay fits for TA kinetic traces of CsPb(Br<sub>0.25</sub>I<sub>0.75</sub>)<sub>3</sub>@SiO<sub>2</sub> QDs. TA spectroscopy was conducted using a 400 nm excitation pump with a fluence of 10  $\mu\text{J}/\text{cm}^2$  and different BuOH exposure times.**

BuOH exposure time (h)	$A_1$	$\tau_1$ (ps)	$A_2$	$\tau_2$ (ps)	$\tau_0$ (ps)	$y_0$
0	0.439	53.2	0.378	350	7.11	0.175
5	0.501	46.5	0.341	307	6.46	0.156
24	0.542	41.6	0.359	297	4.77	0.123
46	0.568	35.0	0.329	285	4.21	0.102
163	0.591	33.5	0.255	271	3.17	0.105

**Table 2. Fitting parameters of bi-exponential decay fits for TA kinetic traces of CsPb(Br<sub>0.25</sub>I<sub>0.75</sub>)<sub>3</sub>@SiO<sub>2</sub> QDs. TA spectroscopy was conducted using a 400 nm excitation pump with a fluence of 20  $\mu\text{J}/\text{cm}^2$  and different BuOH exposure times.**

BuOH exposure time (h)	$A_1$	$\tau_1$ (ps)	$A_2$	$\tau_2$ (ps)	$\tau_0$ (ps)	$y_0$
0	0.429	51.6	0.401	332	10.3	0.161
5	0.485	40.7	0.387	287	9.69	0.131
24	0.519	38.0	0.372	273	7.55	0.114
46	0.528	35.7	0.372	249	5.48	0.119
163	0.550	28.4	0.368	234	5.70	0.0934

In order to clarify the decay processes in the carrier dynamics, a schematic diagram illustrating the phenomena occurring at the carrier-level within PQDs is presented in Fig. 7(c). For simplicity, only three essential carrier decay processes are considered. The first is carrier trapping, represented by a blue solid line box in Fig. 7(c). It indicates that carriers are captured by trap states within the crystal lattice of PQDs [32,33]. The second is radiative carrier recombination, depicted by a green dashed line box. Radiative carrier recombination is a type of bi-molecular (second-order) recombination, and indicates that excited electrons in the CB recombine with holes in the VB, emitting photons with energy corresponding to the PQDs' bandgap [34,35]. The third is trap-assisted non-radiative recombination, illustrated by a yellow dotted line box. This recombination is a type of mono-molecular (first-order) recombination such as geminate [36,37] or Shockley-Read-Hall (SRH) recombination [38–40]. In particular, SRH recombination indicates



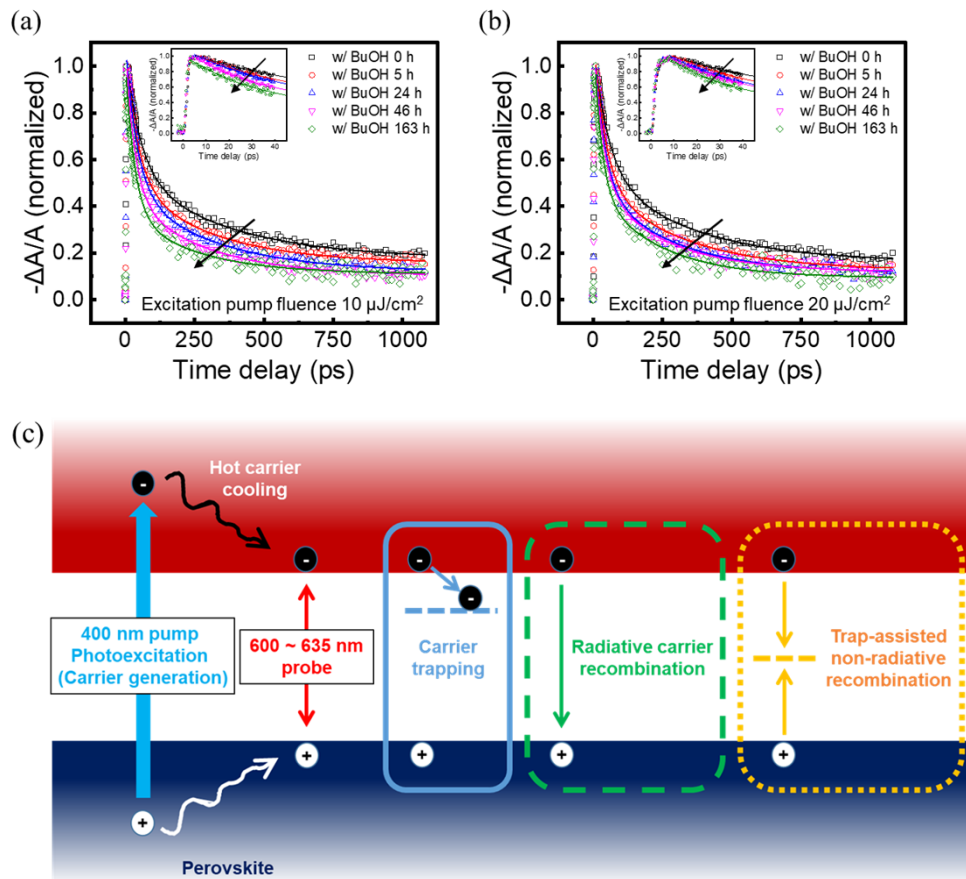


**Fig. 7.** Normalized TA kinetic traces of  $\text{CsPb}(\text{Br}_{0.25}\text{I}_{0.75})_3 @ \text{SiO}_2$  QDs probed at the GSB peaks using a 400 nm excitation pump with fluences of  $10 \mu\text{J}/\text{cm}^2$  (a) and  $20 \mu\text{J}/\text{cm}^2$  (b). Normalized TA kinetic traces obtained from the data in Fig. S5. The solid lines represent the bi-exponential fitting lines. The insets show magnified views of the early-time regime in the TA kinetic traces. (c) Simplified schematic diagram illustrating the carrier dynamics at the carrier-level within PQDs.

that carriers undergo non-radiative recombination through intermediate states. These three decay processes (carrier trapping, carrier radiative combination, and trap-assisted non-radiative recombination) significantly affect the optical properties of PQDs. Consequently, the fast decay mode ( $A_1, \tau_1$ ) corresponds to carrier trapping, while the slow decay mode ( $A_2, \tau_2$ ) corresponds to radiative carrier recombination. The last constant term  $y_0$  is expected to be associated with trap-assisted non-radiative recombination. In that case,  $y_0$  should be originally represented as ( $A_3, \tau_3$ ). Previous studies have reported that trap-assisted non-radiative recombination generally exhibits a recombination lifetime exceeding 10 ns [39,40]. However, in our experiments, the  $y_0$  term show no significant decay since the entire measurement range is limited to at most 1.1 ns. So, it is challenging to accurately determine the kinetics of trap-assisted non-radiative recombination. For this reason, the  $y_0$  parameter was calculated instead of ( $A_3, \tau_3$ ) and was solely used for comparing the fraction of the trap-assisted non-radiative recombination mode in the TA kinetic traces.

To validate the proposed model in Fig. 7(c), a comparative analysis of TA kinetic traces at different excitation pump fluences was conducted. It is because that the TA kinetic traces are expected to change with different pump fluences, considering that the density of photo-induced carriers depends on the excitation fluence, while the number of trap states remains constant at a specific point of BuOH exposure time. Initially, comparisons of the TA kinetic traces with different excitation fluences were conducted to confirm that increasing the excitation fluence leads to an actual increase in the density of photo-induced carriers. Fig. S7a shows the comparison of the TA kinetic traces of PQDs (exposed to BuOH for 0 hours) excited with fluences of 10 and 20  $\mu\text{J}/\text{cm}^2$ , and Fig. S7b shows the result for PQDs exposed for 46 hours. The excitation pump fluence of 10  $\mu\text{J}/\text{cm}^2$  was chosen because it was the minimum fluence that allows for measurements without significant interference from background noise. On the other hand, the pump fluence of 20  $\mu\text{J}/\text{cm}^2$  was selected because the saturation of the TA signal is observed at fluences exceeding 20  $\mu\text{J}/\text{cm}^2$ . In addition, the data of PQDs exposed for 46 hours was selected instead of PQDs with the longest BuOH exposure time (163 hours), because the excessive noise in the TA signal was observed. PQDs exposed to BuOH for 46 hours exhibited sufficient structural degradation and provided a more reliable dataset for our analysis. Based on the results presented in Fig. S7, the TA kinetic traces at each BuOH exposure time exhibit a slight increase when a higher excitation fluence is used, indicating an increase in the photo-induced carrier density.

After discovering that the density of photo-induced carriers increases with an increase of excitation fluence, comparisons of normalized TA kinetic traces with different pump fluences were conducted and shown in Fig. 8. To distinguish two decay modes in the carrier dynamics, the normalized TA kinetic traces were split into two regimes (the early-time regime dominated by carrier trapping and the late-time regime dominated by radiative carrier recombination) and rearranged after breaks in x-axis. The decay lifetimes and coefficient fractions of both decay modes in the TA kinetic traces were also presented in the plots. When the TA kinetic traces were divided into two regimes, it was readily observed that two decay modes in TA kinetics vary in opposite directions as the excitation fluence increases.

In the early-time regime, a decrease in the coefficient  $A_1$  was observed with increasing the excitation fluence. This phenomenon is known as ‘trap state filling’ [41], which indicates that the traps become nearly filled with increased carrier density at high fluence. This can be attributed to both the limited number of trap states and the increased number of photo-induced carriers due to the high excitation fluence. In other words, it is suggested that the carrier trapping effect could be reduced at high pump fluence. Furthermore, it is observed that the magnitude of the decrease in the  $A_1$  coefficient between two excitation fluences increases as BuOH exposure time increases. Specifically, the decrease in  $A_1$  between two excitation fluences is only  $\sim 1\%$  at 0 hours of BuOH exposure time, but it increases to  $\sim 4\%$  at 46 hours. This observation suggests proliferation of trap states by structural degradation during BuOH exposure. Interestingly, the

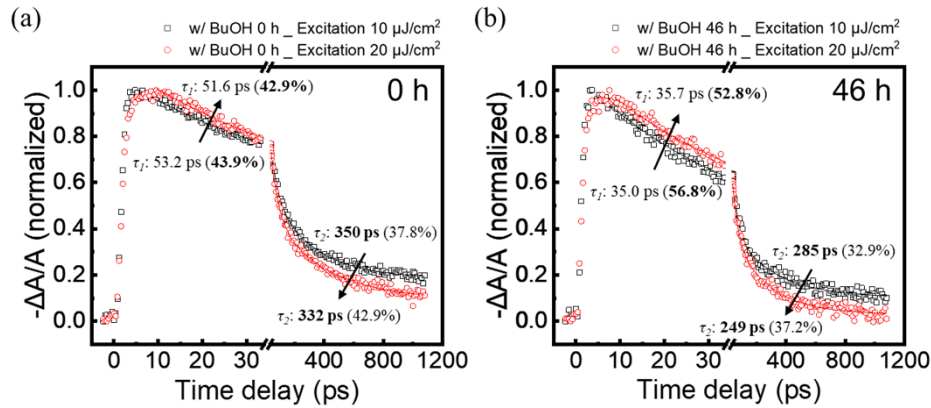


**Fig. 8.** Normalized TA kinetic trace of CsPb(Br<sub>0.25</sub>I<sub>0.75</sub>)<sub>3</sub>@SiO<sub>2</sub> QDs exposed to BuOH for 0 hours (a) and 46 hours (b), probed at the GSB peaks using a 400 nm excitation pump with fluences of 10  $\mu\text{J}/\text{cm}^2$  and 20  $\mu\text{J}/\text{cm}^2$ . The bi-exponential fitting lines and arrows indicating the direction of increasing pump fluence are displayed in plots. The TA kinetic traces are rearranged after x-axis breaks to enhance the clarity of the late-time regime in the pump fluence-dependent TA kinetic traces.

decay lifetime  $\tau_1$  is rarely affected by excitation fluence. The decay lifetime  $\tau_1$  remains relatively constant at  $\sim 50$  ps at 0 hours of BuOH exposure, and  $\sim 35$  ps at 46 hours of BuOH exposure, regardless of the increase in pump fluence. The pump fluence-independence of the decay lifetime of carrier trapping has been reported in a previous study [42].

On the contrast, in the late-time regime, an acceleration in radiative carrier recombination was observed with increasing the excitation fluence. The lifetime  $\tau_2$  decreases from  $\sim 350$  to  $\sim 332$  ps with increasing the excitation fluence at 0 hours of BuOH exposure, and from  $\sim 285$  to  $\sim 249$  ps at 46 hours of BuOH exposure. The pump fluence-dependence of the decay lifetime is one of the most notable characteristics of radiative carrier recombination [43]. Additionally, an increase in the coefficient  $A_2$  was also observed with increasing the excitation fluence. This could be attributed to trap state filling, suggesting that the increased fraction of radiative carrier recombination is expected as a simultaneous result of the decreased fraction in carrier trapping. In other words, increasing the excitation fluence could induce an increase in the fraction of carriers undergoing radiative carrier recombination. Therefore, it was confirmed that the fast and slow decay modes in TA kinetics traces correspond to carrier trapping and radiative carrier recombination, respectively.

Based on the data provided in Table 1 and Table 2, the changes in decay lifetimes ( $\tau_1$  and  $\tau_2$ ) and coefficients ( $A_1$ ,  $A_2$  and  $y_0$ ) under two different excitation pump fluences (10 and 20  $\mu\text{J}/\text{cm}^2$ ) are presented in Fig. 9(a) and (b), respectively. The black solid lines and the red dashed lines in Fig. 9 represent the variations in lifetimes and coefficients under excitation pump fluences of 10  $\mu\text{J}/\text{cm}^2$  and 20  $\mu\text{J}/\text{cm}^2$ , respectively. The results suggest that BuOH exposure leads to both the increase in the fraction of carrier trapping ( $A_1$  increases) and the acceleration in carrier trapping ( $\tau_1$  decreases). Additionally, the fraction of radiative carrier recombination decreases ( $A_2$  decreases), and carrier recombination is accelerated ( $\tau_2$  decreases) with increasing BuOH exposure time. The decrease in the fraction of trap-assisted non-radiative recombination ( $y_0$  decreases) was also observed with increasing BuOH exposure time. The observed decreases in  $A_2$  and  $y_0$  are expected to be induced by the extremely enhanced carrier trapping effects during structural degradation of PQDs. The light-emitting property of PQDs is mainly affected by the carrier density and lifetime of radiative carrier recombination. Our findings clearly demonstrate that BuOH exposure results in  $\text{I}^-$  migration and the formation of carrier trapping states due to

defects within the crystal lattice. As a result, the structural degradation processes of PQDs lead to the reduction in carriers undergoing radiative carrier recombination. Additionally, BuOH exposure also accelerates radiative carrier recombination, indicating a faster escape of carriers from excited states. These factors decrease the number of carriers remaining in excited states and diminish the superior optical characteristics of PQDs, leading to a decline in their light-emitting properties. Nevertheless, we were able to verify that increasing the excitation fluence can reduce the fraction of the carrier trapping mode and increase the radiative carrier recombination mode, indicating a diminishment of the impact of carrier trapping.

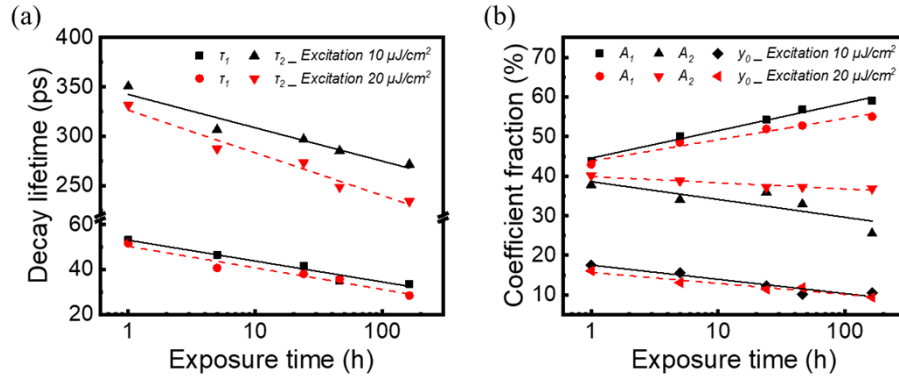


**Fig. 9.** (a) Decay lifetimes and (b) coefficients of bi-exponential decay fits for  $\text{CsPb}(\text{Br}_{0.25}\text{I}_{0.75})_3@ \text{SiO}_2$  QDs as a function of BuOH exposure time. The black solid lines and the red dashed lines represent the variations in lifetimes and coefficients under an excitation pump fluences of  $10 \mu\text{J}/\text{cm}^2$  and  $20 \mu\text{J}/\text{cm}^2$ , respectively.

#### 4. Conclusion

In this study, the changes in the photo-induced carrier dynamics of red-emitting core-shell PQDs during structural degradation caused by exposure to BuOH is investigated using ultrafast TA spectroscopy. When PQDs degraded by exposure to BuOH,  $\text{I}^-$  migration within PQDs was induced, resulting in the formation of trap states due to defects within the perovskite crystal lattice. The increased trap states induced the increase in the number of carriers being trapped, consequently leading to the reduction in carriers undergoing radiative carrier recombination. In addition, BuOH exposure accelerated the decay modes of both carrier trapping and radiative carrier recombination. Consequently, the structural degradation of PQDs led to both the substantial decrease in carrier density undergoing radiative carrier recombination and the rapid departure of carriers from the excited states. These factors hindered the retention of carriers in excited states, resulting in the reduction in the light-emitting properties of PQDs. Nevertheless, it was verified that increasing the excitation fluence can weaken the impact of carrier trapping. At high excitation fluence, the fraction of the carrier trapping mode decreased, and the fraction of the radiative carrier recombination mode increased, because the trap states become occupied by the increased carrier density. These findings contribute a comprehensive understanding of the structural degradation process of PQDs and can aid in the development of PQDs with high structural stability.

**Funding.** National Research Foundation of Korea (NRF-2021R1A2C2093138, NRF-2022R1A2C1010773); Gwangju Institute of Science and Technology (GIST Research Institute (GRI) APRI, GIST Research Institute (GRI) grant).

**Disclosures.** The authors declare no conflicts of interest.

**Data availability.** Data underlying the results presented in this paper are not publicly available at this time but may be obtained from the authors upon reasonable request.

**Supplemental document.** See [Supplement 1](#) for supporting content.

## References

1. A. P. Alivisatos, "Semiconductor Clusters, Nanocrystals, and Quantum Dots," *Science* **271**(5251), 933–937 (1996).
2. Y. Yin and A. P. Alivisatos, "Colloidal nanocrystal synthesis and the organic–inorganic interface," *Nature* **437**(7059), 664–670 (2005).
3. Q. A. Akkerman, G. Rainò, M. V. Kovalenko, and L. Manna, "Genesis, challenges and opportunities for colloidal lead halide perovskite nanocrystals," *Nat. Mater.* **17**(5), 394–405 (2018).
4. C. M. Sutter-Fella, Y. Li, M. Amani, J. W. I. Ager, F. M. Toma, E. Yablonovitch, I. D. Sharp, and A. Javey, "High Photoluminescence Quantum Yield in Band Gap Tunable Bromide Containing Mixed Halide Perovskites," *Nano Lett.* **16**(1), 800–806 (2016).
5. F. Zhao, D. Chen, S. Chang, H. Huang, K. Tong, C. Xiao, S. Chou, H. Zhong, and Q. Pei, "Highly flexible organometal halide perovskite quantum dot based light-emitting diodes on a silver nanowire–polymer composite electrode," *J. Mater. Chem. C* **5**(3), 531–538 (2017).
6. W. Deng, X. Xu, X. Zhang, Y. Zhang, X. Jin, L. Wang, S.-T. Lee, and J. Jie, "Organometal Halide Perovskite Quantum Dot Light-Emitting Diodes," *Adv. Funct. Mater.* **26**(26), 4797–4802 (2016).
7. A. Mohapatra, S. Kumar, T. K. Acharya, C. Goswami, and S. Bhaumik, "Highly stable multi-encapsulated red-emitting cesium lead halide nanocrystals for efficient copper ion detection and imaging in live cells," *J. Alloys Compd.* **947**, 169453 (2023).
8. H. Cho, Y.-H. Kim, C. Wolf, H.-D. Lee, and T.-W. Lee, "Improving the Stability of Metal Halide Perovskite Materials and Light-Emitting Diodes," *Adv. Mater.* **30**(42), 1704587 (2018).
9. C. C. Stoumpos and M. G. Kanatzidis, "Halide Perovskites: Poor Man's High-Performance Semiconductors," *Adv. Mater.* **28**(28), 5778–5793 (2016).
10. C. Sun, Y. Zhang, C. Ruan, C. Yin, X. Wang, Y. Wang, and W. W. Yu, "Efficient and Stable White LEDs with Silica-Coated Inorganic Perovskite Quantum Dots," *Adv. Mater.* **28**(45), 10088–10094 (2016).
11. J. Zhang, L. Zhang, P. Cai, X. Xue, M. Wang, J. Zhang, and G. Tu, "Enhancing stability of red perovskite nanocrystals through copper substitution for efficient light-emitting diodes," *Nano Energy* **62**, 434–441 (2019).
12. Y.-K. Wang, K. Singh, J.-Y. Li, Y. Dong, X.-Q. Wang, J. M. Pina, Y.-J. Yu, R. Sabatini, Y. Liu, D. Ma, J. Liu, Z. Liu, Y. Gao, O. Voznyy, W. Ma, M.-K. Fung, L.-S. Liao, and E. H. Sargent, "In Situ Inorganic Ligand Replenishment Enables Bandgap Stability in Mixed-Halide Perovskite Quantum Dot Solids," *Adv. Mater.* **34**(21), 2200854 (2022).
13. J. Hu, S. Zhang, S. Huang, J. Zhang, M. Lyu, H. Lu, and J. Zhu, "Ligand-mediated CsPbBr<sub>3</sub>–x/SiO<sub>2</sub> quantum dots for red, stable and low-threshold amplify spontaneous emission," *Nanotechnology* **33**(28), 285201 (2022).
14. G. Li, F. W. R. Rivarola, N. J. L. K. Davis, S. Bai, T. C. Jellicoe, F. de la Peña, S. Hou, C. Ducati, F. Gao, R. H. Friend, N. C. Greenham, and Z.-K. Tan, "Highly Efficient Perovskite Nanocrystal Light-Emitting Diodes Enabled by a Universal Crosslinking Method," *Adv. Mater.* **28**(18), 3528–3534 (2016).
15. T. Chiba, Y. Hayashi, H. Ebe, K. Hoshi, J. Sato, S. Sato, Y.-J. Pu, S. Ohisa, and J. Kido, "Anion-exchange red perovskite quantum dots with ammonium iodine salts for highly efficient light-emitting devices," *Nat. Photonics* **12**(11), 681–687 (2018).
16. C. Lee, Y. Shin, A. Villanueva-Antolí, S. Das Adhikari, J. Rodriguez-Pereira, J. M. Macak, C. A. Mesa, S. Giménez, S. J. Yoon, Andrés. F. Gualdrón-Reyes, and I. Mora-Seró, "Efficient and Stable Blue- and Red-Emitting Perovskite Nanocrystals through Defect Engineering: PbX<sub>2</sub> Purification," *Chem. Mater.* **33**(22), 8745–8757 (2021).
17. P. Vashishtha and J. E. Halpert, "Field-Driven Ion Migration and Color Instability in Red-Emitting Mixed Halide Perovskite Nanocrystal Light-Emitting Diodes," *Chem. Mater.* **29**(14), 5965–5973 (2017).
18. J. Hieulle, X. Wang, C. Stecker, D.-Y. Son, L. Qiu, R. Ohmann, L. K. Ono, A. Mugarza, Y. Yan, and Y. Qi, "Unraveling the Impact of Halide Mixing on Perovskite Stability," *J. Am. Chem. Soc.* **141**(8), 3515–3523 (2019).
19. H. Lee, C. K. Trinh, M. G. So, and C.-L. Lee, "Sequential structural degradation of red perovskite quantum dots and its prevention by introducing iodide at a stable gradient concentration into the core–shell red perovskite quantum dots," *Nanoscale* **14**(9), 3425–3440 (2022).
20. L. Wang, C. McCleese, A. Kovalsky, Y. Zhao, and C. Burda, "Femtosecond Time-Resolved Transient Absorption Spectroscopy of CH<sub>3</sub>NH<sub>3</sub>PbI<sub>3</sub> Perovskite Films: Evidence for Passivation Effect of PbI<sub>2</sub>," *J. Am. Chem. Soc.* **136**(35), 12205–12208 (2014).
21. Y. Park, J. Choi, C. Lee, A.-N. Cho, D. W. Cho, N.-G. Park, H. Ihee, and J. Y. Park, "Elongated Lifetime and Enhanced Flux of Hot Electrons on a Perovskite Plasmonic Nanodiode," *Nano Lett.* **19**(8), 5489–5495 (2019).
22. A. M. El-Zohry, B. Turedi, A. Alsalloum, P. Maity, O. M. Bakr, B. S. Ooi, and O. F. Mohammed, "Ultrafast transient infrared spectroscopy for probing trapping states in hybrid perovskite films," *Commun. Chem.* **5**(1), 67 (2022).
23. Y. Park, J. Choi, M. Kang, H. Lee, H. Ihee, and J. Y. Park, "Relaxation Dynamics of Enhanced Hot-Electron Flow on Perovskite-Coupled Plasmonic Silver Schottky Nanodiodes," *J. Phys. Chem. C* **125**(4), 2575–2582 (2021).
24. I.-S. Kim, C. Jo, R. Kang, D.-Y. Kim, S.-J. Son, I.-W. Hwang, and D.-K. Ko, "Fabrication-Method-Dependent Excited State Dynamics in CH<sub>3</sub>NH<sub>3</sub>PbI<sub>3</sub> Perovskite Films," *Sci. Rep.* **7**(1), 16516 (2017).
25. C. Jo, N. J. Jeon, S. J. Lee, C. S. Moon, and D.-K. Ko, "Ultrafast photo-induced carrier dynamics of FAPbI<sub>3</sub>-MAPbBr<sub>3</sub> perovskite films fabricated with additives and a hole transport material," *Chem. Phys. Lett.* **784**, 139100 (2021).



26. F. Zhang, H. Zhong, C. Chen, X. Wu, X. Hu, H. Huang, J. Han, B. Zou, and Y. Dong, "Brightly Luminescent and Color-Tunable Colloidal CH<sub>3</sub>NH<sub>3</sub>PbX<sub>3</sub> (X = Br, I, Cl) Quantum Dots: Potential Alternatives for Display Technology," *ACS Nano* **9**(4), 4533–4542 (2015).
27. J. H. Noh, S. H. Im, J. H. Heo, T. N. Mandal, and S. I. Seok, "Chemical Management for Colorful, Efficient, and Stable Inorganic–Organic Hybrid Nanostructured Solar Cells," *Nano Lett.* **13**(4), 1764–1769 (2013).
28. H. Lee, P. Boonmongkolras, S. Jun, D. Kim, Y. Park, J. Koh, Y.-H. Cho, B. Shin, and J. Y. Park, "In Situ Observation of Photoinduced Halide Segregation in Mixed Halide Perovskite," *ACS Appl. Energy Mater.* **6**(3), 1565–1574 (2023).
29. S. Das, Y. Wang, Y. Dai, S. Li, and Z. Sun, "Ultrafast transient sub-bandgap absorption of monolayer MoS<sub>2</sub>," *Light: Sci. Appl.* **10**(1), 27 (2021).
30. A. Das, K. Marjit, S. Ghosh, D. Ghosh, and A. Patra, "Slowing Down the Hot Carrier Relaxation Dynamics of CsPbX<sub>3</sub> Nanocrystals by the Surface Passivation Strategy," *J. Phys. Chem. C* **127**(31), 15385–15394 (2023).
31. D. Lin, L. Ma, W. Ni, C. Wang, F. Zhang, H. Dong, G. G. Gurzadyan, and Z. Nie, "Unveiling hot carrier relaxation and carrier transport mechanisms in quasi-two-dimensional layered perovskites," *J. Mater. Chem. A* **8**(47), 25402–25410 (2020).
32. Y. Zhang, H. Zhu, J. Zheng, G. Chai, Z. Song, Y. Chen, Y. Liu, S. He, Y. Shi, Y. Tang, M. Wang, W. Liu, L. Jiang, and S. Ruan, "Performance Enhancement of All-Inorganic Perovskite Quantum Dots (CsPbX<sub>3</sub>) by UV-NIR Laser Irradiation," *J. Phys. Chem. C* **123**(7), 4502–4511 (2019).
33. D. Sun, Y. Rao, G. A. Reider, G. Chen, Y. You, L. Brézin, A. R. Harutyunyan, and T. F. Heinz, "Observation of Rapid Exciton–Exciton Annihilation in Monolayer Molybdenum Disulfide," *Nano Lett.* **14**(10), 5625–5629 (2014).
34. S. Mandal, S. Mukherjee, C. K. De, D. Roy, S. Ghosh, and P. K. Mandal, "Extent of Shallow/Deep Trap States beyond the Conduction Band Minimum in Defect-Tolerant CsPbBr<sub>3</sub> Perovskite Quantum Dot: Control over the Degree of Charge Carrier Recombination," *J. Phys. Chem. Lett.* **11**(5), 1702–1707 (2020).
35. C. de Weerd, L. Gomez, A. Capretti, D. M. Lebrun, E. Matsubara, J. Lin, M. Ashida, F. C. M. Spoor, L. D. A. Siebbeles, A. J. Houtepen, K. Suenaga, Y. Fujiwara, and T. Gregorkiewicz, "Efficient carrier multiplication in CsPbI<sub>3</sub> perovskite nanocrystals," *Nat. Commun.* **9**(1), 4199 (2018).
36. C. Wehrenfennig, G. E. Eperon, M. B. Johnston, H. J. Snaith, and L. M. Herz, "High Charge Carrier Mobilities and Lifetimes in Organolead Trihalide Perovskites," *Adv. Mater.* **26**(10), 1584–1589 (2014).
37. Y. Yang, M. Yang, Z. Li, R. Crisp, K. Zhu, and M. C. Beard, "Comparison of Recombination Dynamics in CH<sub>3</sub>NH<sub>3</sub>PbBr<sub>3</sub> and CH<sub>3</sub>NH<sub>3</sub>PbI<sub>3</sub> Perovskite Films: Influence of Exciton Binding Energy," *J. Phys. Chem. Lett.* **6**(23), 4688–4692 (2015).
38. W. Shockley and W. T. Read, "Statistics of the Recombinations of Holes and Electrons," *Phys. Rev.* **87**(5), 835–842 (1952).
39. J. He, A. S. Vasenko, R. Long, and O. V. Prezhdo, "Halide Composition Controls Electron–Hole Recombination in Cesium–Lead Halide Perovskite Quantum Dots: A Time Domain Ab Initio Study," *J. Phys. Chem. Lett.* **9**(8), 1872–1879 (2018).
40. R. L. Milot, G. E. Eperon, T. Green, H. J. Snaith, M. B. Johnston, and L. M. Herz, "Radiative Monomolecular Recombination Boosts Amplified Spontaneous Emission in HC(NH<sub>2</sub>)<sub>2</sub>SnI<sub>3</sub> Perovskite Films," *J. Phys. Chem. Lett.* **7**(20), 4178–4184 (2016).
41. S. D. Stranks, V. M. Burlakov, T. Leijtens, J. M. Ball, A. Goriely, and H. J. Snaith, "Recombination Kinetics in Organic–Inorganic Perovskites: Excitons, Free Charge, and Subgap States," *Phys. Rev. Appl.* **2**(3), 034007 (2014).
42. Z.-Y. Zhang, H.-Y. Wang, Y.-X. Zhang, Y.-W. Hao, C. Sun, Y. Zhang, B.-R. Gao, Q.-D. Chen, and H.-B. Sun, "The Role of Trap-assisted Recombination in Luminescent Properties of Organometal Halide CH<sub>3</sub>NH<sub>3</sub>PbBr<sub>3</sub> Perovskite Films and Quantum Dots," *Sci. Rep.* **6**(1), 27286 (2016).
43. J. S. Manser and P. V. Kamat, "Band filling with free charge carriers in organometal halide perovskites," *Nat. Photonics* **8**(9), 737–743 (2014).